

# Effects of Gravity, Shear and Surface Tension in Internal Condensing Flows: Results From Direct Computational Simulations

Q. Liang

X. Wang

A. Narain

Mem. ASME

e-mail: narain@mtu.edu

Department of Mechanical Engineering-  
Engineering Mechanics,  
Michigan Technological University,  
Houghton, MI 49931

*The paper presents accurate numerical solutions of the full two-dimensional governing equations for steady and unsteady laminar/laminar internal condensing flows. The results relate to issues of better design and integration of condenser-sections in thermal management systems (looped heat pipes, etc.). The flow geometry, in normal or zero gravity, is chosen to be the inside of a channel with film condensation on one of the walls. In normal gravity, film condensation is on the bottom wall of a tilted (from vertical to horizontal) channel. It is found that it is important to know whether the exit conditions are constrained or unconstrained because nearly incompressible vapor flows occur only for exit conditions that are unconstrained. For the incompressible vapor flow situations, a method for computationally obtaining the requisite exit condition and associated stable steady/quasi-steady solutions is given here and the resulting solutions are shown to be in good agreement with some relevant experimental data for horizontal channels. These solutions are shown to be sensitive to the frequency and amplitude of the various Fourier components that represent the ever-present and minuscule transverse vibrations (standing waves) of the condensing surface. Compared to a vertical channel in normal gravity, shear driven zero gravity cases have much larger pressure drops, much slower wave speeds, much larger noise sensitive wave amplitudes that are controlled by surface tension, and narrower flow regime boundaries within which vapor flow can be considered incompressible. It is shown that significant enhancement in wave-energy and/or heat-transfer rates, if desired, are possible by designing the condensing surface noise to be in resonance with the intrinsic waves. [DOI: 10.1115/1.1777586]*

## 1 Introduction

Accurate numerical solutions of the full governing equations are presented for steady and unsteady laminar/laminar film condensation flows on one of the walls inside a channel. This is a good geometry for addressing the influence of shear and gravity by changing the channel inclination from vertical to horizontal (see Fig. 1) and is also a good geometry for consideration of flow behavior in the absence of gravity (space application). The results, based on simulations for channel heights in the 2–25 mm range and a specific choice of 4 mm in Table 1, are important for a qualitative understanding of condenser-section (typically of millimeter or sub-millimeter scale hydraulic diameters) behavior in applications (see Krotiuk [1] and Faghri [2]) such as Looped Heat Pipes, Capillary Pumped Loops, thermal management systems, and electronic-cooling devices.

This channel flow geometry is also a simple modification of the classical flat plate geometry associated with classical studies (Nusselt [3], Rohsenow [4], Koh [5], etc.) for external film condensation over vertical, horizontal, and tilted walls.

To address laminar/laminar flow issues that cannot be addressed by integral approaches (Chow and Parish [6], Narain et al. [7], etc.), direct numerical simulations are undertaken here to better understand the wave-phenomena and associated effects. Although the results presented here are strictly valid only for laminar vapor flows and laminar condensate, in practice, turbulent vapor at inlet (with inlet vapor Reynolds number as large as 7000) is allowed because of the much thicker laminar sub-layer encountered by the vapor flowing in the vicinity of the interface (i.e.,  $y_\delta^+ \gg 5$  as com-

pared to  $y_\delta^+ \approx 5$  which yields the thickness  $y_\delta^+$  of the laminar sub-layer for zero interfacial mass transfer cases—see the definition of nondimensional  $y_\delta^+$  given in terms of the values of  $y^+$  defined in Eq. (6.29) of White [8] and replace the wall shear stress by interfacial shear stress in the expression for nondimensional speed  $u^*$  that appears in this definition). This thickening is due to interfacial mass transfer and associated streamlines that pierce through the interface into a very slow laminar condensate flow. Under these semi-turbulent conditions, the vapor is laminar near the interface and turbulent outside the laminar layer. Therefore, for these cases ( $Re_{in} < 7000$ ), the computational predictions (under laminar/laminar assumptions) of film thickness, heat transfer rates, etc.—though not the predictions for vapor velocity profile outside the interfacial laminar sub-layer—are, as expected, in good agreement with relevant experimental results of Lu [9] and Lu and Suryanarayana [10].

This paper briefly states some of the significant vertical channel results reported in Narain et al. [11] and utilizes its computational methodology to obtain new results for normal gravity (tilted to horizontal channels for gravity to shear dominated flows) and zero gravity. Among other new features of this paper is the fact that surface tension  $\sigma$  is not approximated as a constant (as in [11]) but is taken as  $\sigma = \sigma(T)$  for pure vapor/liquid interface. Furthermore, at the interface, this paper retains the surface tension terms for not only the normal stress condition but also the tangential stress condition (the term responsible for Marangoni effects).

Unconstrained exit-condition cases associated with incompressible vapor flows and constrained exit-condition cases associated with compressible vapor flows physically arise from the fact that condenser-sections (such as the one in Fig. 1) are typically only a part of a closed flow-system (looped heat pipes, etc.) or a closed flow-loop (see, e.g., Fig. 2 in Narain et al. [11]). Therefore, pres-

Contributed by the Heat Transfer Division for publication in the JOURNAL OF HEAT TRANSFER. Manuscript received by the Heat Transfer Division October 4, 2003; revision received April 22, 2004. Associate Editor: J. Chung.

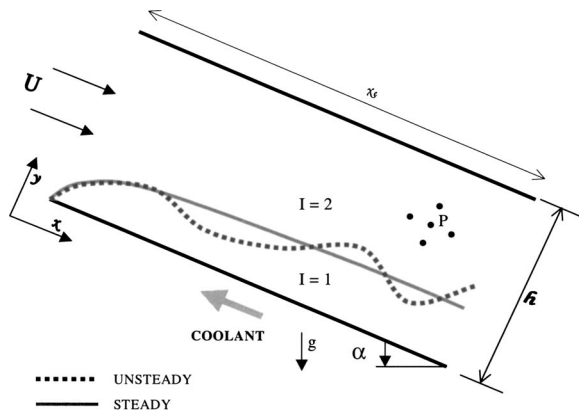


**Fig. 1 Flow geometry for simulations. The film thickness has been exaggerated for the purposes of clarity in discussing the algorithm and the nomenclature. In the figure, all the neighboring points are affecting a flow variable at a typical point P in the “elliptic” vapor flow.**

ence or absence of active flow control (or other constraints) in the remainder of the flow-loop (as is the case in Fig. 2 of [11]) may translate into presence or absence of exit constraints for condenser-section flows (see Fig. 1) under prescribed inlet and wall conditions. The noise-free unsteady simulation method (see Liang [12]) for identifying the correct natural exit condition and the corresponding attractive steady solution which allows nearly incompressible vapor flows (under unconstrained exit conditions) is summarized here briefly, and is given, in greater detail, in Narain et al. [11].

These attractive steady solutions are generally stable to initial disturbances. But, for different gravitational environments, the underlying steady/quasi-steady solutions are attained for quite different natural exit-conditions (i.e., exit vapor quality or exit pressure). However, it is found that the stability for the zero gravity case is weak if the exit condition is not actively held constant at its near natural value (e.g., by the approach indicated in Fig. 2 of [11]).

Also, the sensitivity to minuscule bottom plate noise (that are typically almost always present), is shown to be significantly larger for the flow in zero gravity situations than in normal gravity situations. This is because zero gravity flows have to withstand minuscule persistent noise only with the help of the small surface tension forces present in the normal stress condition. However, for unconstrained-exit cases considered here, these solutions are found to be quite insensitive to noise in the vapor flow at the inlet. Sensitivity to noise at the exit is not considered here but, again, is expected to be large only for certain constrained exit conditions (see Fig. 12 of Narain et al. [11] for discussions regarding the role of vapor compressibility for these cases). It is shown that this noise-sensitivity also depends on the nature of the noise (i.e., its amplitude, frequency, and wave-length content) and the resonance condition effects discussed in Narain et al. [11] for vertical channel configuration are also valid for the other environments considered here (namely the shear dominated horizontal configuration and zero-gravity cases). Furthermore, for gravity dominated

vertical/inclined cases, heat-transfer rates under annular/stratified conditions can easily be enhanced by 10–30 percent for a resonant bottom wall noise that is still minuscule. The enhancements in heat-flux are less significant for zero gravity environments.

For most of the wavy situations considered here for terrestrial environments, the role of surface-tension on the nature of noise-induced waves (phase-speeds, amplitudes, etc.) are found to be negligible. Since small diameter tubes in normal gravity are not considered here, significance of surface tension for that configuration can not be ruled out. As stated earlier, under zero gravity, the role of surface-tension in the normal stress condition at the interface is significant and this result is presented and discussed here. On the other hand, the Marangoni effect of surface tension in the tangential stress condition continues to be negligible for both normal and zero gravity situations—even for nonconstant condensing surface temperatures.

The results presented here underscore the importance of including the role of gravity, exit conditions, and noise-sensitivity issues in categorizing heat transfer correlations and flow regime maps. Therefore currently available heat transfer correlations (Traviss et al. [13]; Shah [14]; etc.) and flow regime maps (see Hewitt et al. [15], Carey [16], etc.) can be improved to address their reported deficiencies (see Palen et al. [17]).

The vapor in the condenser section is considered here to be pure. However, in some applications, noncondensable gaseous impurities may be present. If this is the case, the noncondensables tend to concentrate at the interface (by setting up diffusion processes under appropriate variations in their concentrations and partial pressures) and this usually leads to a significant reduction in heat transfer rates (Minkowycz and Sparrow [18], etc.). In the context of discussions for Fig. 12 in Narain et al. [11] for constrained exit conditions, it was recognized that this situation is prone to instabilities and oscillations due to vapor compressibility effects. It is believed that the presence of noncondensables are likely to provide an extra degree of freedom that will reduce the level of such oscillations/instabilities.

## 2 Governing Equations

The liquid and vapor phases in the flow (e.g., see Fig. 1) are denoted by a subscript  $I: I=1$  for liquid and  $I=2$  for vapor. The fluid properties: density  $\rho$ , viscosity  $\mu$ , specific heat  $C_p$ , thermal conductivity  $k$ , etc., with subscript  $I$ , are assumed to take their representative constant values for each phase ( $I=1$  or 2) and these values for R-113 are obtained here from ASHRAE Handbook [19]. Let  $T_1$  be the temperature fields,  $p_1$  be the pressure fields,  $T_s(p)$  be the saturation temperature of the vapor as a function of local pressure  $p$ ,  $\Delta$  be the film thickness,  $\dot{m}$  be the local interfacial mass flux,  $T_w(x) (< T_s(p))$  be a known temperature variation of the cooled bottom plate, and  $\mathbf{v}_1 = u_1 \hat{\mathbf{i}} + v_1 \hat{\mathbf{j}}$  be the velocity fields (where  $\hat{\mathbf{i}}$  and  $\hat{\mathbf{j}}$  denote unit vectors along  $x$  and  $y$  axes). Furthermore, let  $h$  be the channel height,  $g_x$  and  $g_y$  be the components of gravity along  $x$  and  $y$  axes,  $p_0$  be the inlet pressure,  $\Delta T \equiv T_s(p_0) - T_w(0)$  be a representative controlling temperature difference between the vapor and the bottom plate,  $h_{fg}$  be the heat of vaporization at temperature  $T_s(p)$ ,  $\sigma$  be the surface tension at any temperature  $T_s(p)$  with  $\sigma_0$  being the specific value at  $T_s(p_0)$ , and  $U$  be the average inlet vapor speed determined by the inlet mass flux. With  $t$  representing the physical time and  $(x,y)$  representing

**Table 1 Specification of reported flow situations involving saturated R-113 vapor at the inlet. Properties of R-113 are taken from ASHRAE Handbook [19].**

Fig. # for flow	$p_0$ (kPa) $Re_{in}$	$T_s(p_0)$ ( $^{\circ}C$ ) Ja	$\Delta T$ ( $^{\circ}C$ ) $Fr_x^{-1}$	$h$ (m) $Fr_y^{-1}$	$U$ (m/s) $\rho_2/\rho_1$	$\sigma^*$ (N/m) $\mu_2/\mu_1$	We	$Pr_1$
3, 5a–5d, 6, 7, 8a–8b, 9, 10, 11a–11b, 12a–12b, 13	108.855 1200	49.47 0.0341	5 0.2379	0.004 $0.32 \times 10^{-6}$	0.41 0.0053	0.015 0.0209	67.6	7.2236

physical distances of a point with respect to the axes in Fig. 1 ( $x=0$  is at the inlet and  $y=0$  is at the condensing surface), we introduce a new nondimensional list of the fundamental variables through the following definitions

$$\{x, y, \delta, u_I, \dot{m}\} \equiv \left\{ \frac{x}{h}, \frac{y}{h}, \frac{\Delta}{h}, \frac{u_I}{U}, \frac{\dot{m}}{\rho_1 U} \right\} \quad (1)$$

$$\{v_I, \theta_I, \pi_I, t\} \equiv \left\{ \frac{y_I}{U}, \frac{T_I}{\Delta T}, \frac{p_I - p_0}{\rho_I U^2}, \frac{t}{(h/U)} \right\}$$

The nondimensional differential forms of mass, momentum ( $x$  and  $y$ -components), and energy equations for flow in the interior of either of the nearly incompressible phases ( $I=1$  or  $2$ ) are the well-known equations

$$\frac{\partial u_I}{\partial x} + \frac{\partial v_I}{\partial y} = 0$$

$$\frac{\partial u_I}{\partial t} + u_I \frac{\partial u_I}{\partial x} + v_I \frac{\partial u_I}{\partial y} = - \left( \frac{\partial \pi_I}{\partial x} \right) + Fr_x^{-1} + \frac{1}{Re_I} \left( \frac{\partial^2 u_I}{\partial x^2} + \frac{\partial^2 u_I}{\partial y^2} \right) \quad (2)$$

$$\frac{\partial v_I}{\partial t} + u_I \frac{\partial v_I}{\partial x} + v_I \frac{\partial v_I}{\partial y} = - \left( \frac{\partial \pi_I}{\partial y} \right) + Fr_y^{-1} + \frac{1}{Re_I} \left( \frac{\partial^2 v_I}{\partial x^2} + \frac{\partial^2 v_I}{\partial y^2} \right)$$

$$\frac{\partial \theta_I}{\partial t} + u_I \frac{\partial \theta_I}{\partial x} + v_I \frac{\partial \theta_I}{\partial y} \approx \frac{1}{Re_I Pr_I} \left( \frac{\partial^2 \theta_I}{\partial x^2} + \frac{\partial^2 \theta_I}{\partial y^2} \right)$$

where  $Re_I \equiv \rho_I U h / \mu_I$ ,  $Pr_I \equiv \mu_I C_{pI} / k_I$ ,  $Fr_x^{-1} \equiv g_x h / U^2$  and  $Fr_y^{-1} \equiv g_y h / U^2$ . The above equations are solved for each of the two phases under a complete and proper prescription of boundary conditions (inlet, exit, and the walls), initial conditions, and the interface conditions (see Delhay [20], etc.). These conditions are used in their exact forms and they are given in Eqs. (3)–(15) and Eqs. (A1)–(A9) of Narain et al. [11].

An inspection of all the nondimensional governing equations, interface conditions, and boundary conditions reveal the fact that the flows considered here are affected by the following set of nondimensional parameters

$$\left\{ Re_{in}, Ja, Fr_x^{-1}, \frac{\rho_2}{\rho_1}, \frac{\mu_2}{\mu_1}, Pr_1, x_e, Z_e(0), We, Fr_y^{-1} \right\} \quad (3)$$

where  $Re_{in} \equiv \rho_2 U h / \mu_2 \equiv Re_2$ ,  $Ja \equiv C_{p1} \Delta T / h_{fg}^0$ , and  $h_{fg}^0 \equiv h_{fg}(T_s, p_0)$ . Here  $Re_{in}$ ,  $Fr_x^{-1}$ , and  $Ja$  are control parameters associated with inlet speed  $U$ , inclination  $\alpha$ , and temperature difference  $\Delta T$ . For unconstrained exit condition cases (i.e., incompressible vapor) considered here, it is seen later that  $Z_e(0)$ , the initial value of the exit vapor quality, is not important because it does not affect the naturally selected steady solution and its associated exit vapor quality  $Z_e|_{Na}$ . The density ratio  $\rho_2 / \rho_1$ , viscosity ratio  $\mu_2 / \mu_1$ , and Prandtl number  $Pr_1$  are passive fluid parameters. Also, for unsteady or quasi-steady wavy-interface situations, the normal stress condition at the interface imply an additional dependence on a surface tension parameter, Weber number  $We \equiv \rho_1 U^2 h / \sigma$ . For superheated vapors, in the interface energy equation, there is a very weak dependence on the thermal conductivity ratio  $k_2 / k_1$ . Furthermore, unlike in Narain et al. [11], in this paper, nonconstant surface tension  $\sigma = \sigma(T)$  for pure vapors is allowed through  $\nabla_s \sigma$  term in Eq. (A3) in the appendix of [11]. As a result, the term  $[t]$  on the right side of the tangential stress condition given in Eq. (5) of [11] is modified by adding an additional term “ $Ma \partial \pi_2 / \partial x |^i \cdot 1 / \sqrt{1 + \delta_x^2}$ ” on the right side of Eq. (A9) of [11]. Here the Marangoni number  $Ma \equiv \rho_2 U c_1 d_1 / \mu_1$  represents the surface tension contribution to tangential stress under the notation  $c_1 \equiv dT_s / dp$  and  $d_1 \equiv -d\sigma / dT$ . For the cases considered here, a representative set of values of the new constants are:  $c_1 \approx 0.0003$  K/Pa,  $d_1 \approx 0.1046$  N/(m-K), and  $Ma = 0.1963$ .

It should be noted that negligible interfacial thermal resistance and equilibrium thermodynamics on either side of the interface is assumed to hold for values of  $x$  downstream of the origin (i.e., second or third computational cell onwards). And hence, as per discussions leading to Eq. (A8) in the appendix of Narain et al. [11], no model (see, Carey [16], Plesset and Prosperetti [21], etc.) is needed to supplement the known restrictions on the interfacial mass-flux  $\dot{m}$  (see Eq. (8) of Narain et al. [11]). However, reasonable initial estimates (from Nusselt [3] solution, etc.) for  $\dot{m}$  are used to obtain convergent solutions that are eventually shown to be independent of the initial guess.

Though  $x \sim 0$  zone does not affect the results of this paper, ability to account for interfacial thermal resistances does become important when the liquid-vapor phase-change interface lies within 10–500 nm of a solid surface that is at a temperature different than the phase-change saturation temperature (say by more than 5°C). At such locations, boiling or condensation processes do require development of relevant thermodynamics and material-science knowledge base (suitably supported by experiments and molecular dynamic simulations) that would yield models of the type described in Carey [16], Plesset and Prosperetti [21], etc. This is an area of modern research that may provide key technological insights with regard to some key relevant processes (such as control of nucleation sites in boiling, sustenance of drop-wise condensation, etc.).

By dropping all time dependencies in the initial boundary value problem described above, the resulting steady equations (which are elliptic near exit) for any reasonable but arbitrarily prescribed exit condition  $Z_e$  (denoted as an initial value of  $Z_e(t)$  at  $t=0$ ), where

$$Z_e(0) = \int_{\delta_{steady}(x_e)}^1 u_2(x_e, y) \cdot dy \equiv Z_e \quad (4)$$

the steady solution is obtained. This solution is then assumed to apply at times  $t \leq 0$ . That is, if  $\phi(x, y, t)$  is any variable (such as  $u_I$ ,  $v_I$ ,  $\pi_I$ ,  $\theta_I$ , etc.), the initial values of  $\phi$  and film thickness  $\delta(x, t)$  are such that

$$\phi(x, y, 0) = \phi_{steady}(x, y) \quad \text{and} \quad \delta(x, 0) = \delta_{steady}(x) \quad (5)$$

where  $\phi_{steady}$  and  $\delta_{steady}$  represent steady solutions. Although the prescription of  $Z_e$  within  $0 < Z_e < 1$  is arbitrary (except that it should be such that it allows a steady computational solution in the stratified/annular regime assumed in Fig. 1), its natural value (denoted as  $Z_e|_{Na}$ ) for the unconstrained cases is computationally found by the procedure outlined in section 4.

Using the initial condition in (5), the unsteady solutions for  $t > 0$  are obtained by solving the full initial boundary value problem with appropriate boundary conditions (with or without the typically present minuscule vibrations of the condensing surface). Since an assumption of unconstrained exit conditions (i.e., incompressible vapor) are made for the unsteady computations in this paper, no exit conditions are prescribed for  $t > 0$  as long term values of the exit condition (such as  $Z_e|_{Na}$  for steady noise-free situations) are obtained as part of the solution.

### 3 Features of the Computational Approach

Details of the computational approach are given in Narain et al. [11] and Liang [12]. Some essential features and a broad outline are summarized here.

Between times “ $t$ ” and “ $t + \Delta t$ ,” two types of adaptive grids (termed grid-A and grid-B) are employed. At time  $t$ , grid-A (see Fig. 3 of [11]) is based on a stair-step geometrical approximation of  $\delta(x, t)$  as a function of  $x$  and it changes whenever the liquid and the vapor flow variables need to be recomputed for a changed interfacial configuration  $\delta(x, t)$ . The physical processes, however, employ a piecewise linear or higher (cubic splines) approximation of  $\delta(x, t)$  based on their discrete values at marked locations in grid-A. In the interior of either the liquid or the vapor phase,

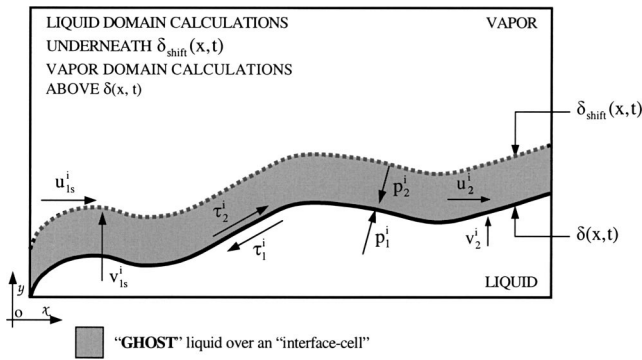


**Fig. 2** The liquid domain calculations underneath  $\delta_{\text{shift}}(x,t)$  with prescribed values of  $(u_{1s}^i, v_{1s}^i, \theta_{1s}^i)$  on  $\delta_{\text{shift}}(x,t)$  satisfy the shear and pressure conditions on the actual  $\delta(x,t)$ . Discarding all other calculations, only calculations underneath  $\delta(x,t)$  are retained. The vapor domain calculations above  $\delta(x,t)$  with prescribed values of  $(u_2^i, v_2^i, \theta_2^i)$  on  $\delta(x,t)$  satisfy  $\dot{m}_{VK} = \dot{m}_{\text{Energy}}$  and the requirement of continuity of tangential velocities.

grid-A is used for all calculations. However, to make the best changes in  $\delta(x,t)$  leading to its accurate prediction at time “ $t + \Delta t$ ,” a different grid (grid-B) is generated for spatially locating the variables ( $\delta(x,t)$ ,  $\bar{u}(x,t)$ , and  $\bar{v}(x,t)$ ) that appear in the interface tracking equation (see Eq. (7) below) for this problem. As discussed and shown in Fig. 3 of Narain et al. [11], grid-B needs to be defined for the  $x$ -domain alone because it is employed for the specific purpose of obtaining the best numerical predictions for changes in  $\delta(x,t)$  through Eq. (7) described later on in this paper. The predictions made on grid-B are interpolated to obtain corresponding values on grid-A. At any time  $t$ , linear mappings suffice for spatial interpolation and exchange of the values of the relevant flow variables (viz.  $\delta$ ,  $\bar{u}$ , and  $\bar{v}$ ) at locations between grid-A and grid-B. The approach broadly consists of the following:

- At discrete number of locations in Fig. 2, guess  $\{\delta, u_{1s}^i, v_{1s}^i, \theta_{1s}^i, u_2^i, v_2^i, \theta_2^i\}$ .
- Under the shifted interface depicted in Fig. 2, the liquid domain problem is solved by a finite-volume method (SIMPLER utilizing source term method described in Patankar [22] and Narain et al. [11]).
- Above the interface, the vapor domain problem (see Fig. 4(b) of [11]) is also solved by a finite-volume method (SIMPLER utilizing source term method described in Patankar [22] and Narain et al. [11]).
- The seven guesses are repeatedly updated to converge to their correct values with the help of seven interface conditions given in Narain et al. [11] (one each from Eqs. (3)–(5), two from Eq. (8), and two from Eq. (9) of [11]). For the steady problem for  $t=0$ , the exit condition  $Z_e$  needs to be prescribed and an additional eighth “condition” is created to satisfy this requirement.
- The above steps are repeated in such a way that all interface conditions, differential equations, etc., are satisfied.

One of the interface conditions, viz. the physical variable form of  $\dot{m}_{LK} = \dot{m}_{\text{Energy}}$  in Eq. (8) of [11], also given as one of the equalities in Eq. (A7) of [11], is rewritten, with the help of Eqs. (A1) and (A5) of [11], in its popular interface tracking equation form

$$\frac{\partial H}{\partial t} + \mathbf{v}_1^i \cdot \nabla H \cong \frac{-k_1}{\rho_1 \cdot h_{fg}} \frac{\partial T_f^i}{\partial n} \cdot |\nabla H| \quad (6)$$

When the right side of Eq. (6) is zero, spatial extension of Eq. (6) leads to a color function  $H$  whose initial values  $H=0$  and  $H=1$  within each of the phases are retained for all times  $t > 0$ , and this forms the basis of the popular VOF (volume of fluids) techniques

(see Hirt and Nicholas [23], etc.) for air/water type flows. Similarly, a suitable spatial extension of Eq. (6), in conjunction with some other techniques, is used in the Level-Set method (Sussman et al. [24], etc.) for capturing the interface through iterative single-domain (consisting of both the phases) calculations. For boiling related phase change flows, the Level-Set technique has recently been used by Son and Dhir [25]. In order to overcome some of the problems (see, e.g., Li and Renardy [26]) associated with interface capturing techniques (be it Level-Set, VOF, etc.) that utilize Eq. (6), the limited goal here was to ensure that these problems do not give rise to spurious computationally generated waves when no physical disturbances or noise are present. This difficult requirement was met by looking at the existing knowledge base for the reduced form of Eq. (6) given in Eq. (7) below. By substituting  $H = h \cdot \{y - \delta(x,t)\}$ ,  $\partial H / \partial t = -U \cdot \partial \delta / \partial t$ ,  $\partial H / \partial x = -\partial \delta / \partial x$ ,  $\partial H / \partial y = 1$ , etc. in Eq. (6) and properly nondimensionalizing the resulting equation, one obtains the following interface tracking problem

$$\frac{\partial \delta}{\partial t} + \bar{u}(x,t) \frac{\partial \delta}{\partial x} = \bar{v}(x,t) \quad (7)$$

$$\delta(0,t) = 0$$

$$\delta(x,0) = \delta_{\text{steady}}(x) \text{ or other prescriptions}$$

where  $\bar{u} \equiv u_1^i + \{Ja / (\text{Re}_1 \cdot \text{Pr}_1)\} \partial \theta_1 / \partial x^i$  and  $\bar{v} \equiv v_1^i + \{Ja / (\text{Re}_1 \cdot \text{Pr}_1)\} \partial \theta_1 / \partial y^i$  typically depend strongly, but indirectly, on  $\delta$ . The computational issues for discretization and numerical solution of Eq. (7) are well understood and discussed in Narain et al. [11].

The computational approach defined above meets the following requirements: (i) the convergence criteria (i.e., smallness of “ $b$ ” defined on p. 125 of Patankar [22]) in the interior of each fluid is satisfied, (ii) all the interface conditions are satisfied, (iii) grid independent solutions are obtained for grids that are sufficiently refined (see Fig. 14 of [11]), (iv) unsteady simulations yielding the sensitive interface locations are free of computational noise (this is achieved by ensuring that there is an absence of computational noise in the absence of physical noise), and (v) its predictions for the classical steady problems of condensation on vertical or horizontal plates (Nusselt [3], Koh [5], etc.) are in agreement (see Narain et al. [11] and Yu [27]) with the classical solutions. As per estimates described in Narain et al. [11], the sum total of errors in the solutions reported here is less than 6 percent.

#### 4 Identification of Steady/Quasi-Steady Solutions and Their Compatibility With Experiments

For slow laminar/laminar internal condensing flows considered here, the steady governing equations are such that the behavior of the  $x$ -component of the velocity field are “elliptic” in the sense that downstream conditions are able to affect flow variables at an upstream location (see a representative point P in Fig. 1). This behavior of the steady equations allow the signature of degeneracy associated with a stationary saturated mixture in a closed container (i.e., the fluid, under equilibrium thermodynamics conditions, could have many vapor/liquid interfacial configurations associated with different mixtures—from all vapor to all liquid—with the actual quality being determined by the total amount of heat removed from an initial all vapor configuration) to be carried over to the steady solutions of the governing equations and one has many steady interfacial configurations for different exit-conditions (i.e., different exit vapor qualities  $Z_e$  in Eq. (4)) that represent different amounts of heat removed for any given inlet and wall conditions. As a result, as is seen in Fig. 5 of [11], there are different steady solutions for different exit vapor qualities. However, for incompressible steady vapor flows associated with unconstrained-exit cases, unsteady noise-free simulations in Fig. 3 (which are free of both physical and computational noise) show that these steady solutions seek out a naturally selected exit condition (denoted as  $Z_e|_{\text{Na}}$ ) as  $t \rightarrow \infty$ . In other words, there is an

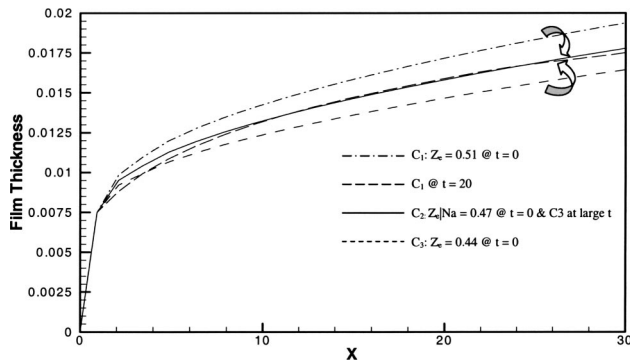


**Fig. 3** For flow situation specified in Table 1 with  $\alpha=90$  deg and  $x_e=30$ , the figure depicts two sets of steady solutions  $C_1$  (for  $Z_e=0.51$ ) and  $C_3$  (for  $Z_e=0.44$ ) that provide the initial conditions for solutions to be obtained for  $t>0$  without any specification of exit conditions. The figure shows the resulting  $\delta(x,t)$  predictions for  $t>0$ , the set of  $\delta(x,t)$  curves  $C_1$  start at  $Z_e=0.51$  at  $t=0$ , and tend, as  $t \rightarrow \infty$ , to the solution for which  $Z_{e|Na}=0.47$ . The other set of curves  $C_3$  start at  $Z_e=0.44$  at  $t=0$  and also tend, as  $t \rightarrow \infty$ , to the same  $Z_{e|Na}$  solution.

attracting wave-free steady solution, which, in the qualitative representation of Fig. 4(a), is termed an attractor. The definition of an attractor among the steady solutions of a well-posed initial boundary value problem for a system of partial differential equations is qualitatively the same as that of a stable node (see Greenberg [28]) among the stationary solutions of a system of nonlinear ordinary differential equations. As shown later, this solution is stable but sensitive to noise. As a result, in practice, only a quasi-steady wavy solution of the type indicated in Fig. 4(b) is actually realized.

Since the above procedure requires consideration of the unsteady equations to identify the natural steady solution, it is obvious that this approach is both novel and different from steady incompressible single-phase or air/water flows where it typically suffices to work with steady equations to obtain steady solutions. The above approach for identifying stable quasi-steady incompressible vapor solutions is also found to be in good agreement (see Tables 2 and 3) with relevant experimental results of Lu [9] and Lu and Suryanarayana [10]. These experiments were done under unconstrained-exit conditions and filmwise condensation on the bottom surface of a horizontal duct (length=0.91 m) of rectangular cross-section (width=40 mm, height=25 mm). For comparisons with the simulations, the flow in the vertical midsection

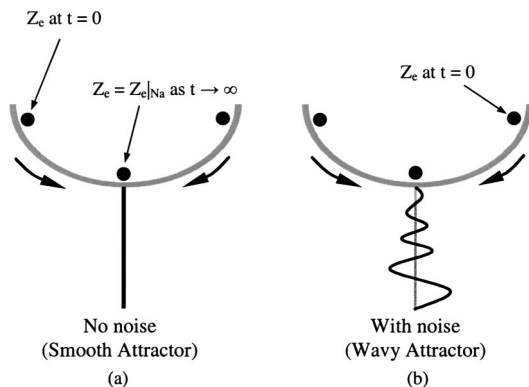


**Fig. 4** Qualitative nature of the attracting steady/quasi-steady solution. The figure shows that different steady solutions associated with different exit conditions ( $Z_e$  at  $t=0$ ) are attracted, under unconstrained exit conditions and as  $t \rightarrow \infty$ , to a special steady solution with  $Z_e=Z_{e|Na}$ .

**Table 2** Comparison of experimental and computational  $Z_{e|Na}$  values<sup>1</sup>

Run #		$Z_e @ x_e = 12$	$Z_e @ x_e = 24$	$Z_e @ x_e = 36$	Mean Error %
220	Expt.	0.776	0.572	0.477	-2.13
	Theory	0.81	0.58	0.48	
221	Expt.	0.828	0.702	0.583	5.85
	Theory	0.85	0.66	0.5	
100	Expt.	0.908	0.824	0.761	-0.17
	Theory	0.92	0.84	0.74	
181	Expt.	0.884	0.796	0.718	3.97
	Theory	0.89	0.76	0.66	

<sup>1</sup>Flow of saturated R113 condensing on the bottom plate of a horizontal channel of  $h=25$  mm,  $x_e=0.91$  m and measurements of  $Z_{e|Na}$  at  $x_e=12, 24$ , and  $36$ .

of the experimental geometry (where ultrasound film thickness sensors, etc. were mounted) is modeled as a two-dimensional horizontal channel flow (with gap height  $h=25$  mm). Furthermore, for experimental runs considered in Tables 2 and 3, the simulations ensured that the fluid (refrigerant called R-113), the average inlet velocity in the channel, bottom/top channel wall temperatures, and inlet pressure were specified to be the same as the specifications/values of the corresponding items/variables in the selected experimental runs. It is found in Tables 2 and 3 that, for horizontal channel flows considered, good agreement was obtained well beyond the typical laminar/laminar restriction of inlet vapor Reynolds number (based on channel height as characteristic length) being approximately less than 2000. It was found that the agreement was good for inlet vapor Reynolds number up to 7000. Perhaps, because of slow laminar condensate flows ( $Re_\delta < 150$ , where  $Re_\delta$  is defined in Incropera and DeWitt [29]) and nonzero interfacial mass transfer through inclined or transverse vapor streamlines near the interface, the condensing vapor develops a sufficiently thick laminar sub-layer in the vicinity of the interface (see Narain et al. [11] or Liang [12]). This laminar layer allows computational predictions of film thickness, heat transfer rates, etc. under overall laminar/laminar assumptions to continue to remain in good agreement with the experiments of Lu and Suryanarayana [10] (though, perhaps, predictions of vapor velocity profile outside the laminar sub-layer of the vapor above the interface may not be good).

**Effects of Gravity on Natural Steady Solutions.** In Fig. 5(a) we see that gravity has a significant influence on film thickness. In the absence of gravity assisted condensate drainage that occurs for vertical/inclined configurations, condensate film is much thicker in zero gravity. However, zero gravity condensate is still slightly thinner than its values for the corresponding horizontal configuration. This is because, in the horizontal configuration, part of the vapor shear is used to deny the tendency of the condensate's hydrostatic-pressure distribution to cause a backward downhill flow and only the remaining vapor shear is used to keep it forward moving with a monotonically increasing film thickness. This monotonic increase of condensate thickness is due to a net balance that occurs between continuous accumulation of the liquid (under condensation mass transfer across the interface) and its forward flow. Despite the proximity of the horizontal and zero-gravity steady solutions, the absence of the transverse gravitational force in zero gravity makes the pressure variations in the liquid much more sensitive to the surface tension term in the normal stress condition (the second term on the right side of Eq. (4) in [11]) and this, as we see in the next section, causes much larger amplitude interfacial waves in response to ever present condensing surface noise. The significance of the magnitude of the transverse gravitational restoring force is best seen by observing that the liquid pressure variations  $\pi_1(x,y,t)$  is affected both by its interfacial value  $\pi_1^i$  (as given by Eq. (4) in [11]) and its value required by the  $y$ -component of the momentum equation in Eq. (2). For example, if effects of  $v_1(x,y,t)$  is ignored because of its smallness, the

**Table 3 Comparison of experimental and computational mean film thickness values<sup>1</sup>**

Flow Speed U (m/s)	Run #	$\Delta T(^{\circ}C)$		$\delta(x_1)$	$\delta(x_2)$	$\delta(x_3)$	$\delta(x_4)$	$\delta(x_5)$	Average % Error
0.34	220	31.21	Expt.	0.010	0.015	0.016	0.018	0.020	-5%
			Comp.	0.012	0.014	0.015	0.017	0.019	
0.31	221	21.42	Expt.	0.008	0.013	0.014	0.015	0.017	2.9%
			Comp.	0.011	0.013	0.014	0.016	0.018	
0.42	100	14.76	Expt.	0.012	0.014	—	0.015	0.015	4.2%
			Comp.	0.010	0.013	—	0.016	0.018	
0.5	181	21.42	Expt.	0.008	0.012	0.013	0.014	0.016	3.0%
			Comp.	0.009	0.012	0.013	0.015	0.016	

<sup>1</sup>Flow of saturated R113 condensing on the bottom plate of a horizontal channel of  $h=25$  mm,  $x_e=0.91$  m and measurements of film thickness values at  $x=2.03, 6.10, 10.16, 18.29,$  and  $32.51$ .

y-momentum balance in Eq. (2) implies  $\pi_1(x, y, t) \cong \pi_1^i + |Fr_y^{-1}|(\delta - y)$ , where  $|Fr_y^{-1}|$  is a positive constant and  $\pi_1^i$  satisfies Eq. (4) of [11].

Furthermore, Fig. 5(b) shows it is equivalent to prescribe exit pressure ( $\bar{\pi}_2 \equiv 1/(1-\delta) \int_0^{\delta} \pi_2 dy$ ) or exit quality  $Z_e$  at  $x=x_e$  and that the natural exit conditions (exit quality  $Z_{e|Na}$  or associated exit pressure) are different in different gravitational environments. The shear dominated cases (horizontal and zero gravity) have a much larger pressure drop and hence have a much narrower flow regime within which the compressibility of the vapor can be ig-

nored (this is because an increase in  $\Delta p_2/p_0$  makes the underlying assumption " $\Delta \rho_2/\rho_{20} \ll 1$ " a poorer approximation). Figure 5(c-d) show that phase-speeds  $\bar{u}_{steady}(x)$  (see Narain et al. [11]) for zero gravity and horizontal configurations are significantly smaller than gravity driven vertical cases, and, as a result, in Fig. 5(d), the characteristics curves along which disturbances propagate (see Narain et al. [11]) become very nearly vertical. This means that, for these shear dominated cases, effects of condensing surface noise are likely to accumulate around the location of the noise.

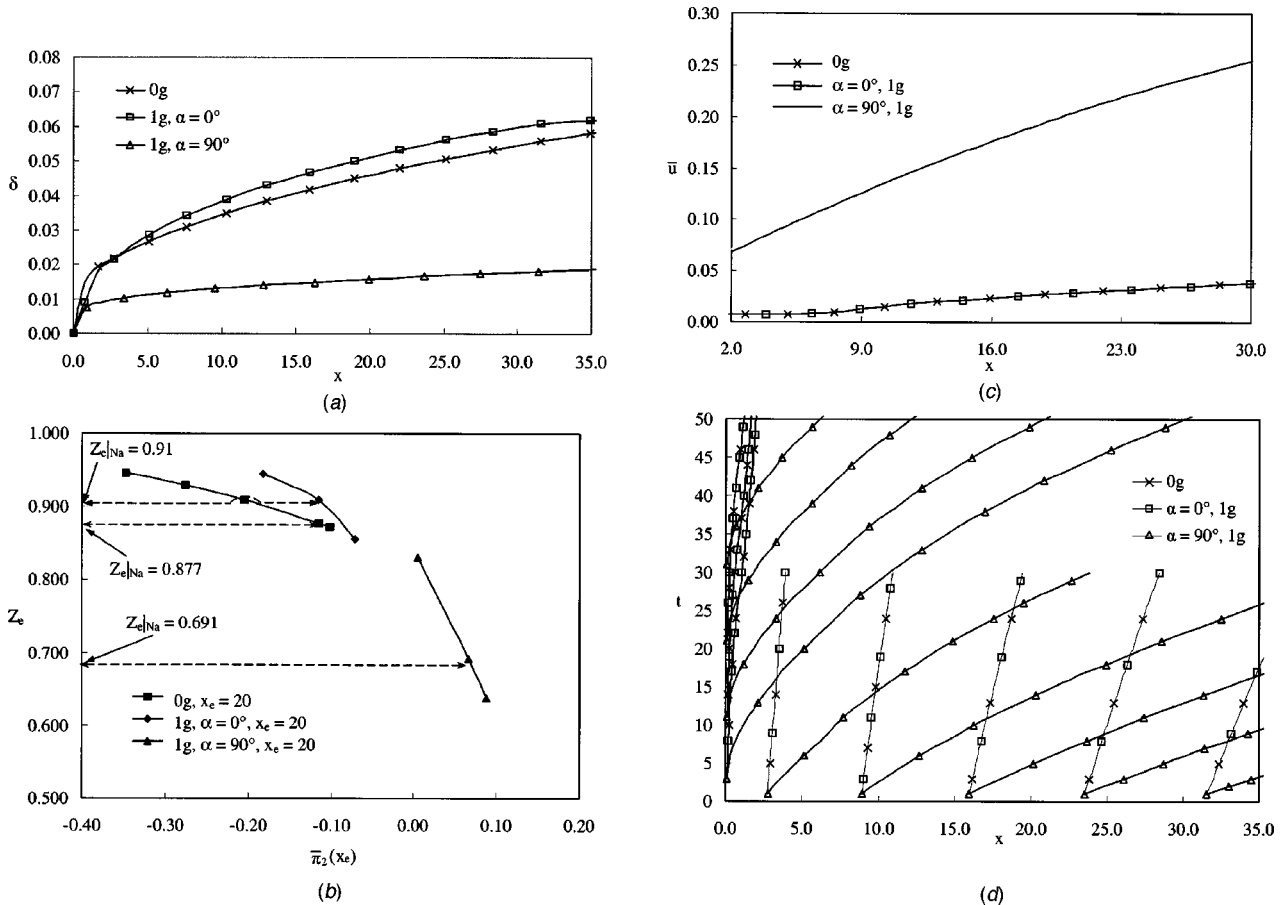


**Fig. 5 (a)** For flow situations specified in Table 1, the figure shows smooth steady condensate film thickness for vertical, horizontal and zero-gravity cases which have, for  $x_e=20$ ,  $Z_{e|Na}=0.691, 0.877,$  and  $0.91$  respectively. **(b)** For the flow situations specified in Table 1, the figure shows different exit pressure  $\bar{\pi}_2(x_e)$  values associated with different  $Z_e$  values. In particular, it also shows  $Z_{e|Na}$  and their corresponding exit pressure values for the cases considered in Fig. 5(a). **(c)** For flow situations specified in Table 1, the figure shows phase-speeds  $\bar{u}_{steady}(x)$  for the cases considered in Fig. 5(a). **(d)** For flow situation specified in Table 1, the characteristics curves  $x=x_e(t)$  denote curves along which infinitesimal initial disturbances naturally propagate (see [11]) on the stable steady solutions of Fig. 5(a). On characteristics that originate on  $x=0$  line, there are no disturbances as  $\delta(0,t) \cong 0$  implies  $\delta' \cong 0$ .

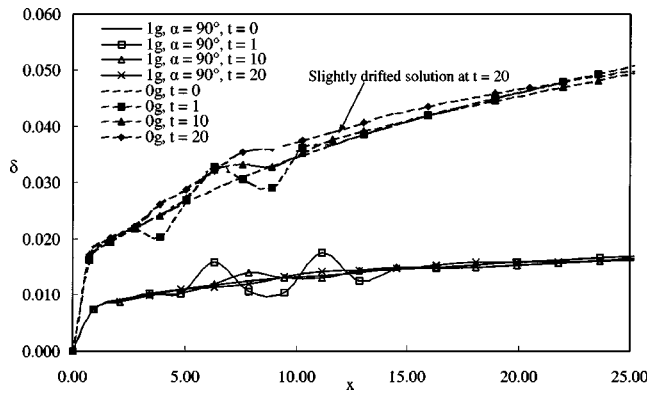


**Fig. 6** For flow situations specified in Table 1, the above  $\delta(x, t)$  predictions ( $\Delta t = 10$ ) are for vertical and 0g cases with initial data  $\delta(x, 0) = \delta_{\text{steady}}(x) + \delta'(x, 0)$ , where a nonzero disturbance  $\delta'(x, 0)$  has been superposed at  $t = 0$  on the steady solution  $\delta_{\text{steady}}$ . Here  $\delta'(x, 0) = 0.004 \cdot \sin(2\pi x/5)$  for  $3.5 \leq x \leq 13.5$  and  $\delta' = 0$  elsewhere.

## 5 Discussion of Unsteady Simulation Results

**Effects of Initial Disturbance.** The behavior of natural exit-condition and associated smooth-interface steady solutions as obtained in Fig. 3 are qualitatively described in Fig. 4. In normal gravity, as shown in Narain et al. [11], these solutions are intrinsically wavy but stable to initial disturbances. However the stability of the natural ( $Z_e = Z_e|_{\text{Na}}$ ) smooth-interface zero gravity solutions, as compared to stability of normal gravity solutions, is demonstrated by the results in Fig. 6. In Fig. 6, there is some separation between the  $t \rightarrow \infty$  (i.e., large  $t$ , or  $t = 20$ ) and  $t = 0$  solutions for the zero gravity case. As the size of the amplitude of the disturbance used for the zero gravity case in Fig. 6 was reduced, it was found that the  $t \rightarrow \infty$  (i.e., large  $t$ , or  $t = 20$ ) solution stayed closer to the  $t = 0$  solution associated with the natural exit condition. This large time behavior implies that the stability for the zero gravity case, as compared to normal gravity case, is weak. In other words, loosely speaking, for qualitative purposes, the bowl at the bottom of Fig. 4(a) is much flatter for zero gravity than the corresponding cases for normal gravity. This weak stability in zero gravity is observed even in the absence of surface tension and momentum transfer terms in the interfacial normal stress condition given in Eq. (4) of [11]. Therefore the weak stability to initial disturbances is a result of the mass transfer and the associated nature of the streamlines (which, at the interface, are more transverse in gravity driven flows and more slanted, as in Fig. 7, for shear dominated flows) rather than stabilizing or destabilizing effects of surface tension and/or momentum-transfer terms in the normal stress condition at the interface (see the right side of Eq. (4)).

**Effects of Noise and Resonance.** The noise-sensitivity of the solutions in Fig. 5(a) is shown in Figs. 7 and 8. These Figures show that the interface is quite sensitive to even minuscule standing wave vibrations of the bottom plate given by  $v_1(x, 0, t) = \varepsilon \cdot \sin(2\pi x/\lambda) \cdot \sin(2\pi t/T)$  whose amplitude  $\varepsilon$  is in the range of  $10^{-5} - 3 \cdot 10^{-5}$ . This, in a way, is expected from Eq. (7) because interfacial disturbances are forced by the interfacial value  $v_1'$  of the transverse velocity  $v_1$  that appears in  $\bar{v}$ . Furthermore, the extreme smallness of this forcing is consistent with the fact that, on average,  $u_2 \gg u_1 \gg v_1$  with each dominance being at least two to three orders of magnitude (i.e.,  $10^2$  or  $10^3$ ) bigger over the other. For the cases considered here (e.g., the case of  $T \approx 24$ ,  $\lambda \approx 10$ ,  $h \approx 0.004$  m, and  $U \approx 0.41$  m/s), the maximum displacement amplitude of the vibrations are about  $0.25 \mu\text{m}$ , maximum velocity amplitude are about  $0.12 \mu\text{m/s}$ , and maximum accelera-

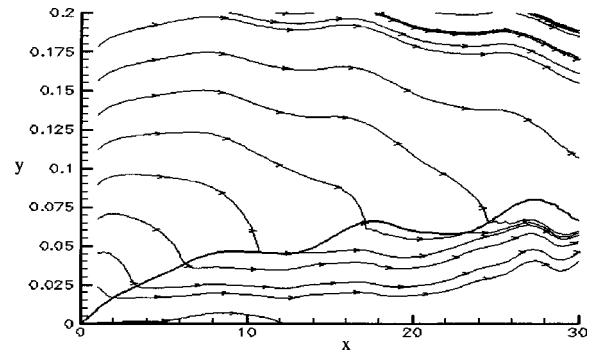


**Fig. 7** Closer to the interface, the figure shows the interface location and vapor/liquid streamlines at  $t = 300$  for a resonant bottom wall noise given as  $v_1(x, 0, t) = \varepsilon \cdot \sin(2\pi x/\lambda) \cdot \sin(2\pi t/T)$  where  $\varepsilon = 0.32E-5$ ,  $\lambda = 10$ , and  $T(x) = \lambda/\bar{u}_{\text{steady}}(x)$ . The underlying steady solution is for a zero gravity flow in Table 1 with  $x_e = 30$ ,  $Z_e|_{\text{Na}} = 0.91$  and  $\sigma_0 = 15E-03$  N/m.

tion amplitude are about  $6.25 \cdot 10^{-4} \text{ m/s}^2$  (which is less than  $10^{-4}g$ ,  $g \approx 10 \text{ m/s}^2$ ). Such vibrations are indeed commonly present as structural or coolant flow induced vibrations and these are in the 0–30 Hz range considered here. For the wavy cases discussed/studied here, these vibrations are often the primary cause of observed interfacial oscillations. Although the results shown in Figs. 7 and 8 are for sinusoidal standing waves on the condensing surface at  $y = 0$ , more complex two-dimensional or three-dimensional patterns will arise from a more general noise that would typically be present. Even if the noise itself is two-dimensional, any three-dimensional imperfection in the geometry can cause the waves to become three-dimensional.

For the resonance cases (vertical, horizontal, and zero-gravity) considered in Fig. 8(a) the resonance phenomena comes into play (see Narain et al. [11]) when the external noise frequency  $f_{\text{ext}}$  and wavelength  $\lambda$  associated with minuscule standing-wave noise of the bottom plate are chosen such that:

$$\lambda f_{\text{ext}}(x) \cong \bar{u}_{\text{steady}}(x) \quad (8)$$

where the steady problem's phase speeds  $\bar{u}_{\text{steady}}(x)$  in Eq. (8) is well defined (see Fig. 5(c)) and is known from the steady solution for  $Z_e = Z_e|_{\text{Na}}$ . At a chosen operating condition, this large rate resonance condition can be actively achieved by placing vibration actuators along the condensing surface with well-defined frequency shifts or by a passive design (suitable variations in material thickness and/or composition) of the plate associated with the condensing surface. For zero gravity, the resonant noise-induced waves in Fig. 8(a) lead to enhanced pressure drops (see Fig. 8(b)).

The above-described effects of bottom wall standing-wave noise employ a product of a single wavelength spatial sinusoid and a single-frequency temporal sinusoid. In practice, there are several sinusoidal components of different wavelengths and frequencies. Once the actual components of bottom wall noise is experimentally known (with the help of accelerometers) and modeled (say as  $v_1(x, 0, t)|_I = 2\varepsilon \cdot \sin(2\pi x/\lambda) \cdot \sin(2\pi t/T)$  and  $v_1(x, 0, t)|_{II} = \varepsilon \cdot \sin(2\pi x/\lambda) \cdot \sin(2\pi t/T) + \varepsilon \cdot \sin(2\pi x/(\lambda/2)) \cdot \sin(2\pi t/T)$  in Fig. 9), the resulting shapes of the different free surface waves (see Fig. 9) and their effects can be assessed. Experimental measurements of both the bottom wall noise and real time film thickness values can be used for further validation and use of the resonance phenomena.

In Fig. 10, the waves in 0g (for  $\sigma = \sigma_0$ ) have significantly greater amplitude for noise amplitude of  $\varepsilon = 5\varepsilon^*$  as opposed to  $\varepsilon = \varepsilon^*$ . This is because forward wave speeds are very small and higher accumulation rates of local interfacial disturbances at higher amplitudes significantly dominate the damping rates of lo-

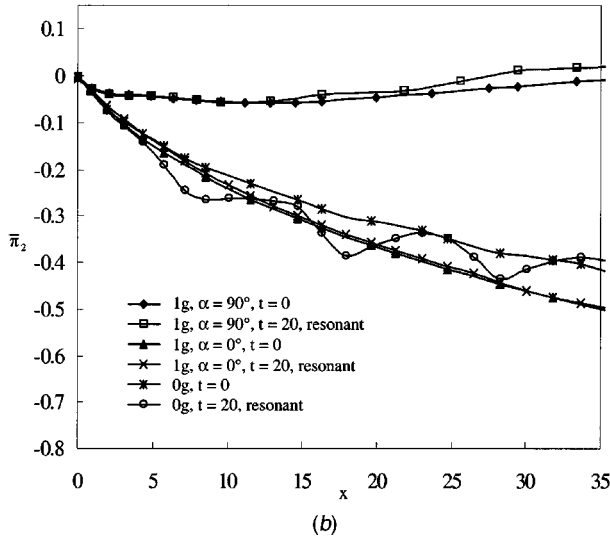
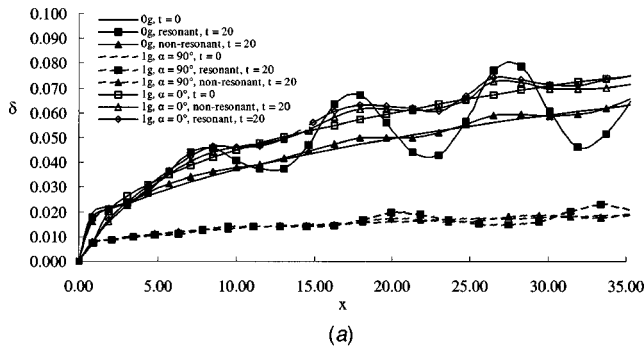


**Fig. 8** (a) For flow situations specified in Table 1 and  $x_e=35$ , the above  $\delta(x,t)$  values at  $t=0$  (with  $Z_e=Z_{elNa}$ ) and  $t=20$  are for resonant and non-resonant bottom wall noise given as  $v_1(x,0,t)=\varepsilon \cdot \sin(2\pi x/\lambda) \cdot \sin(2\pi t/T)$ ,  $\varepsilon=0.24E-05$  and  $\lambda=10$ . For nonresonant cases  $T=24$  and for resonant cases  $T=T(x)=\lambda/\bar{u}_{steady}$ . (b) For flow situations specified in Table 1 and  $x_e=35$ , the steady and unsteady values of exit pressures are shown as a function of  $x$ . The predictions are for case 1: vertical ( $\alpha=90$  deg), case 2: horizontal in 1g ( $\alpha=0$  deg,  $Fr_y^{-1}=0.233$ ) and case 3: 0g ( $Fr_y^{-1}=0$ ). The waves are due to bottom wall noise specified in Fig. 8(a).

cal disturbances. In the next section it is seen that surface tension forces eventually contain these larger amplitudes.

**Effects of Surface Tension.** For typical interfacial waviness associated with vertical to horizontal cases in the presence of gravity (e.g., the vertical case in Fig. 8(a)), it is found that the surface tension and momentum transfer terms in the relation for interfacial pressures (viz. the second and third terms on the right side of Eq. (4) in [11]) do not play a role over most of the condensing surface (a small leading edge zone over  $0 \leq x \leq \varepsilon_0$ , with  $\varepsilon_0 \ll 1$ , is excluded because flow physics in this region do not affect the rest of the flow). This was computationally verified. For example, in Fig. 8(a), waves for vertical and horizontal configurations, remain essentially the same (within 1–2 percent) as surface tension  $\sigma$  takes values over  $0 \leq \sigma \leq 100\sigma^*$  and the momentum transfer term in Eq. (4) of [11] is retained or dropped. In other words, on earth, the value of the forcing  $v_1^i$  (see the right side of Eq. (7)) that influences  $\delta$  is dominated, through  $\pi_1(x,y,t)$ , by gravitational forces  $|Fr_x^{-1}|$  and/or  $|Fr_y^{-1}|$  and surface tension is not influential. The interfacial value of  $v_1(x,y,t)$ , denoted as  $v_1^i$ , is influenced by  $\pi_1(x,y,t)$  values which in turn are affected both by the interfacial liquid pressure  $\pi_1^i$  (see the surface tension term on the right side of Eq. (4) in [11]) and the  $x$  and  $y$ -momentum

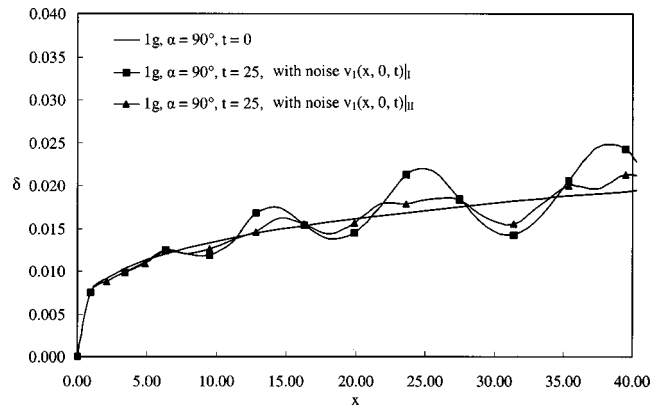


**Fig. 9** For flow situations specified in Table 1, the  $\delta(x,t)$  values at  $t=0$  (with  $Z_e=Z_{elNa}$ ) and  $t=25$  are for different bottom wall noises defined as:  $v_1(x,0,t)|_I=2\varepsilon \cdot \sin(2\pi x/\lambda) \cdot \sin(2\pi t/T)$ , and  $v_1(x,0,t)|_{II}=\varepsilon \cdot \sin(2\pi x/\lambda) \cdot \sin(2\pi t/T) + \varepsilon \cdot \sin(2\pi x/(\lambda/2)) \cdot \sin(2\pi t/T)$  where  $\varepsilon=0.24E-05$ ,  $\lambda=10$ ,  $T=T(x)=\lambda/\bar{u}_{steady}$ , and  $\sigma_0=0.015$  N/m.

balance equations in Eq. (2) that play a role in the motion of the condensate. However, as seen in Fig. 8(a), effects of surface tension forces, in the interfacial normal stress condition (see Eq. (4) of [11]) are not masked in zero gravity where the surface tension term provides a key effect (which, for typically small surface tension values, becomes more significant whenever the curvature or  $\delta_{xx}$  values become large). Thus surface tension particularly plays a significant role in 0g response to bottom wall noise of amplitude above certain values (compare  $\varepsilon=\varepsilon^*$  with  $\varepsilon=5\varepsilon^*$  for non-resonant 0g cases in Fig. 10). This is because higher noise amplitudes cause accumulation of interfacial disturbances to exceed their removal/damping rates and an unsteady situation is attained where the wave amplitudes are contained by just the right variations in curvature that are consistent with the role of surface tension forces in the normal stress condition. Furthermore, in Fig. 10, it is seen that the above-described dynamics is such that there is a wave amplitude decrease as surface tension values increase (for  $\sigma_0=30\sigma^*$ ) and a wave amplitude increase with decrease in surface tension (for  $\sigma_0=\sigma^*/30$ ). Computations also verify that an assumption of a hypothetical zero surface tension at the interface does not allow zero gravity flows to withstand average values of wall heat flux ( $q_w''=-k_1 \cdot \partial T_1 / \partial y|_{y=0}$ ) are only slightly higher

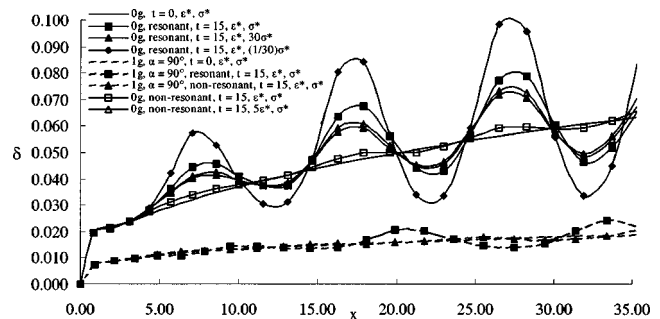


**Fig. 10** For flow situations specified in Table 1, the  $\delta_{steady}(x)$  and  $\delta(x,t)$  predictions are for resonant and nonresonant bottom wall noise with different amplitudes  $\varepsilon$  ( $\varepsilon^*$  or  $5\varepsilon^*$ ) and different surface tensions  $\sigma_0$  ( $\sigma^*$  or  $30\sigma^*$  or  $\sigma^*/30$ ). The noise in the legend are specified by  $v_1(x,0,t)=\varepsilon \cdot \sin(2\pi x/\lambda) \cdot \sin(2\pi t/T)$ ,  $\varepsilon^*=0.24E-05$ ,  $\lambda=10$ , and  $\sigma^*=0.015$  N/m. For nonresonant cases,  $T=24$  and for resonant cases,  $T=T(x)=\lambda/\bar{u}_{steady}$ .

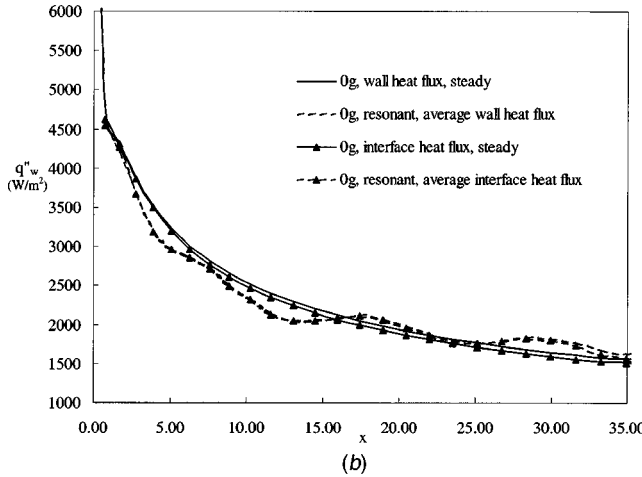
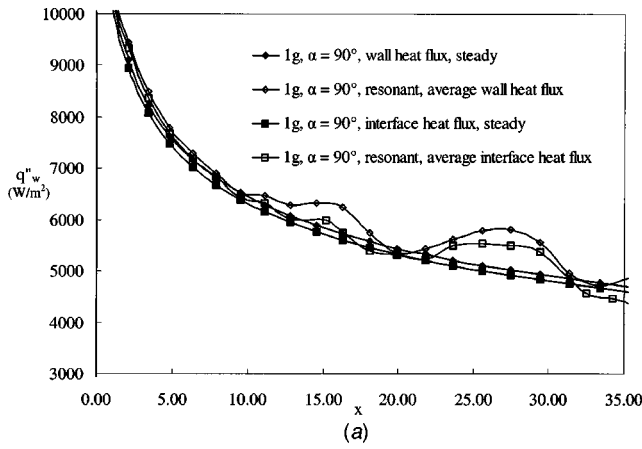


**Fig. 11** (a) For the flow situations specified in Table 1,  $x_e = 35$ , and vertical configuration; the figure shows steady and time-averaged values of heat flux at the wall and at the interface; and (b) for the flow situations specified in Table 1,  $x_e = 35$ , and 0g configuration; the figure shows steady and time-averaged values of heat flux at the wall and at the interface

than time averaged values of interfacial heat-flux ( $q''_i \equiv -k_1 \cdot \partial T_1 / \partial n|_i$ ). This is because transverse conduction heat transfer significantly dominates sensible cooling (i.e., mean liquid temperature drops somewhat with distance  $x$ ).

It is recalled that heat transfer rates can also be increased under constrained exit conditions associated with compressible vapor flows—e.g., by increasing the exit pressure (or decreasing  $Z_e$  from 0.50 to 0.38 in Fig. 5 of [11]). The noise sensitivity analyses and flow regime (e.g., plug/churn versus annular flows) issues for these constrained cases are not studied here and are not fully understood at this point.

**Effects on Shear Stress.** Effects of noise-induced persistent waves are best reported as mean interfacial tangential stress  $\bar{T}_{nt_0}^i$  on a representative or mean steady location  $\delta_{\text{steady}}(x)$  of the interface ( $\delta(x,t) \equiv \delta_{\text{steady}}(x) + \delta'(x,t)$ ). Replacing  $\delta_{\text{steady}}(x)$  by steady interfacial location at  $t=0$  (obtained, as in Fig. 5(a), under noise-free conditions for exit condition  $Z_e = Z_{e|Na}$ ), a mean tangential stress (over time duration  $[t_i, t_f]$ , where  $t_i$  and “ $t_f - t_i$ ” are sufficiently large times) along the unit tangent  $\hat{t}_0(x)$  at  $x$  is defined as

$$\bar{T}_{nt_0}^i \equiv \frac{1}{(t_f - t_i)} \int_{t_i}^{t_f} \{\mathbf{T}_1^i \hat{\mathbf{n}} \cdot \hat{\mathbf{t}}_0\} \circ dt \equiv \rho_1 U^2 \cdot \bar{\tau}_{nt_0}^i, \quad (9)$$

where  $\mathbf{T}_1^i$  is the stress tensor value at the liquid interface ( $\mathbf{T}_1^i \equiv -p_1^i \mathbf{1} + \mathbf{S}_1^i$ ) and  $\hat{\mathbf{n}}$  is the unit normal on the interface (see defi-

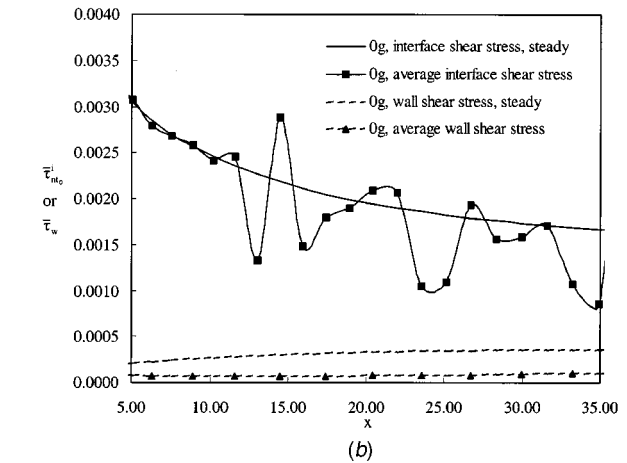
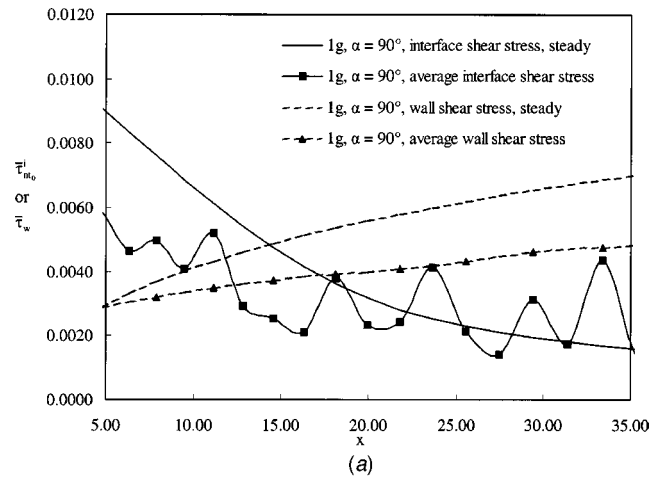


**Fig. 12** (a) For the flow situations specified in Table 1,  $x_e = 35$ , and vertical configuration; the figure shows steady and time-averaged values of shear stress at the wall ( $\bar{\tau}_w$ ) and the tangential stress ( $\bar{\tau}_{nt_0}^i$ ) at the steady interface location; and (b) For the flow situations specified in Table 1,  $x_e = 35$ , and 0g configuration; the figure shows steady and time-averaged values of shear stress at the wall ( $\bar{\tau}_w$ ) and the tangential stress ( $\bar{\tau}_{nt_0}^i$ ) at the steady interface location

nitions given in the appendix of [11]). Clearly  $\bar{\tau}_{nt_0}^i$  in Eq. (9) is the nondimensional value of the physical stress  $\bar{T}_{nt_0}^i$ . On the bottom wall, at  $y=0$ , with unit vectors  $\hat{\mathbf{n}} = \hat{\mathbf{j}}$  and  $\hat{\mathbf{t}}_0 = \hat{\mathbf{i}}$ ; the nondimensional wall shear stress  $\bar{\tau}_w$  is similarly defined.

The interfacial and wall shear values are shown in Figs. 12(a,b). Under influence of gravity, as the condensate speeds up in Fig. 12(a), gravity driven waves cause a shear enhancement. It was verified that this enhancement is primarily due to viscous stresses and the pressure-drag contribution in Eq. (9) is very small. On the contrary, in the shear-dominated situation in Fig. 12(b), gravitational energy is not available; and, as a result, waves slightly decrease the mean interfacial shear as more of the instantaneous energy imparted to the condensate by the instantaneous values of the interfacial shear stress (i.e., vapor exerted traction on the liquid) must be used to sustain fluctuations on the liquid interface. However, unlike Fig. 12(a), in shear-dominated cases of Fig. 12(b), interfacial shears are much larger relative to wall shears.

**Effects of Nonconstant Wall Temperatures.** In most applications, the condensing surface temperature  $T_w(x)$  is not a constant. As shown in Fig. 13, all else remaining the same, two different wall temperature variations  $T_w(x)$  lead to predictions of

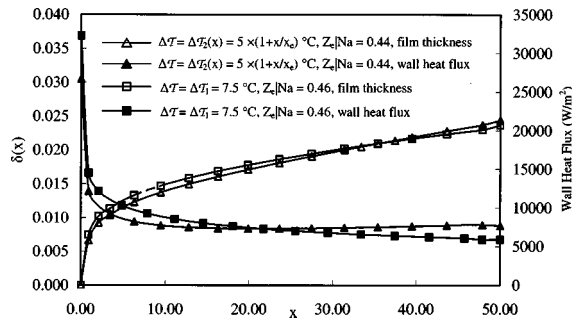


**Fig. 13** For flow situation specified in Table 1 with  $\alpha=90$  deg and  $x_e=50$ , the above figure depicts two different film thickness, wall heat flux, and natural exit condition  $Z_{e|Na}$  predictions for two different wall temperature specifications  $T_w(x)$  (and hence  $\Delta T$ ) which is, for case 1:  $\Delta T_1=7.5^\circ\text{C}$  and case 2:  $\Delta T_2(x)=5^\circ\text{C}\cdot(1+x/x_e)$

natural exit conditions  $Z_{e|Na}$  which are somewhat different but close to one another because both temperature variations have the same average value between the inlet and the exit. As a consequence, as is seen in Fig. 13, on average, both the condensate thickness and wall heat flux values are also reasonably close to one another.

## 6 Conclusions/Results

In addition to a brief summary of the algorithm and vertical channel results reported in Narain et al. [11], the new results reported here are:

- For unconstrained exit conditions, the effectiveness (by way of showing compatibility with known experiments) of the unsteady noise-free simulation method for identifying the natural exit condition and associated attracting steady solution has been demonstrated for the shear-dominated cases (zero gravity and horizontal configurations) as well.
- The nonresonant and resonant effects of ubiquitous minuscule bottom plate vibrations on the stable steady solutions are demonstrated here for shear-dominated cases (zero gravity and horizontal configurations) and compared with the earlier results for gravity dominated vertical case.
- It is shown that, for suitably large (yet minuscule) amplitude bottom wall vibrations, the ability to sustain condensing surface noise in zero gravity is due only to normal stress effects of surface tension. Furthermore it is shown that zero gravity cases show significantly higher accumulation of noise-induced disturbances resulting in higher amplitude waves as compared to similarly induced waves in terrestrial environments.
- Effects of surface tension were shown to be insignificant for terrestrial environments (horizontal to vertical).
- Effects of surface tension in the tangential stress condition (the Marangoni effects) are found to be negligible in all environments.
- A weaker stability and higher noise-sensitivity of the zero gravity steady solutions is demonstrated. It is inferred that an active control for holding the natural exit condition fixed, active reductions in condensing surface noise levels, an increase in normal stress on the liquid interface by electrical or other means, etc. are needed for stable realizability of annular condensing flows in space-based applications.
- The proposed computational method's ability to predict significant flow variables (streamlines, interfacial and wall values of shear and heat-flux, etc.) for constant and non-constant wall temperatures is demonstrated.

The above results provide an understanding that is necessary for further enhancement of the reported simulation methods and codes. Future enhancements will allow considerations of: vapor compressibility effects for constrained exit cases, simulations for

longer channels and thicker condensates, and more general handling of the interface tracking equation (Eq. (6)) that allows predictions of phenomena that exhibit interfacial pinch-off and droplet formations.

## Acknowledgment

This work was partially supported by the NSF grant CTS-0086988, and a grant (NNCO4GB52G) from NASA office of Biological and Physical Sciences.

## Nomenclature

- $C_p$  = specific heat, J/(kg-K)  
 $h$  = gap between the plates (see Fig. 1), m  
 $h_{fg}$  = latent heat ( $h_g - h_f$ ), J/kg  
 $Ja$  = Jacob number,  $C_{p1}\Delta T/h_{fg}$   
 $k$  = thermal conductivity, W/(m-K)  
 $p$  = pressure, N/m<sup>2</sup>  
 $p_0$  = pressure at the inlet, N/m<sup>2</sup>  
 $q_w''$  = bottom wall heat flux at any point and time, W/m<sup>2</sup>  
 $Re_1$  = Reynolds numbers  $\rho_1 U h / \mu_1$   
 $Re_{in}$  = inlet Reynolds number  $Re_2$   
 $T$  = temperatures, K  
 $\Delta T$  = temperature difference between the vapor and the wall, K  
 $U$  = value of the average vapor speed at the inlet, m/s  
 $(u, v)$  = values of x and y components of velocity, m/s  
 $(u, v)$  = nondimensional values of u and v  
 $(x, y, t)$  = physical distances along and across the bottom plate and time, (m, m, s)  
 $(x, y, t)$  = nondimensional values of (x, y, t)  
 $Z_e$  = ratio of exit vapor mass flow rate to total inlet mass flow rate

## Greek Symbols

- $\delta$  = nondimensional value of condensate thickness  
 $\Delta$  = physical value of condensate thickness, m  
 $\varepsilon$  = amplitude of nondimensional disturbances representing values of  $v_1(x, 0, t)$   
 $\mu$  = viscosity, Pa-s  
 $\nu$  = kinematic Viscosity  $\mu/\rho$ , m<sup>2</sup>/s  
 $\pi$  = nondimensional pressure  
 $\rho$  = density, kg/m<sup>3</sup>  
 $\sigma$  = surface tension, N/m  
 $\theta$  = nondimensional temperature  
 $\bar{\tau}_w$  = steady or time-averaged nondimensional wall shear stress  
 $\bar{\tau}_{nt_0}^i$  = steady or time-averaged nondimensional tangential shear stress at a point on a steady interface location

## Subscripts

- $I$  = it takes a value of 1 for liquid phase and 2 for vapor phase  
 $s$  = saturation condition  
 $w$  = wall

## Superscripts

- $i$  = value of a variable at an interface location

## References

- [1] Krotuk, W. J., 1990, *Thermal-Hydraulics for Space Power, Propulsion, and Thermal Management System Design*, American Institute of Aeronautics and Astronautics, Inc., Washington, D.C.
- [2] Faghri, A., 1995, *Heat Pipe Science and Technology*, Taylor and Francis, Washington D.C.
- [3] Nusselt, W., 1916, "Die Oberflächenkondensation des Wasserdampfes," *Z. Ver. Dt. Ing.*, **60**(27), pp. 541–546.
- [4] Rohsenow, W. M., 1956, "Heat Transfer and Temperature Distribution in Laminar Film Condensation," *Trans. ASME*, **78**, pp. 1645–1648.
- [5] Koh, J. C. Y., 1962, "Film Condensation in a Forced-Convection Boundary-Layer Flow," *Int. J. Heat Mass Transfer*, **5**, pp. 941–954.

- [6] Chow, L. C., and Parish, R. C., 1986, "Condensation Heat Transfer in Micro-Gravity Environment," *Proceedings of the 24th Aerospace Science Meeting*, AIAA, New York.
- [7] Narain, A., Yu, G., and Liu, Q., 1997, "Interfacial Shear Models and Their Required Asymptotic Form for Annular/Stratified Film Condensation Flows in Inclined Channels and Vertical Pipes," *Int. J. Heat Mass Transfer*, **40**(15), pp. 3559–3575.
- [8] White, F. M., 2003, *Fluid Mechanics*, Fifth Edition, McGraw Hill.
- [9] Lu, Q., 1992, "An Experimental Study of Condensation Heat Transfer With Film Condensation in a Horizontal Rectangular Duct," Ph.D. thesis, Michigan Technological University.
- [10] Lu, Q., and Suryanarayana, N. V., 1995, "Condensation of a Vapor Flowing Inside a Horizontal Rectangular Duct," *ASME J. Heat Transfer*, **117**, pp. 418–424.
- [11] Narain, A., Liang, Q., Yu, G., and Wang, X., 2004, "Direct Computational Simulations for Internal Condensing Flows and Results on Attainability/Stability of Steady Solutions, Their Intrinsic Waviness, and Their Noise-Sensitivity," *ASME J. Appl. Mech.*, **71**, pp. 69–88.
- [12] Liang, Q., 2003, "Unsteady Computational Simulations and Code Development for a Study of Internal Film Condensation Flows' Stability, Noise-Sensitivity, and Waviness," Ph.D. thesis, Michigan Technological University.
- [13] Traviss, D. P., Rohsenow, W. M., and Baron, A. B., 1973, "Forced-Convection Condensation Inside Tubes: A Heat Transfer Equation for Condenser Design," *ASHRAE J.*, **79**, Part 1, pp. 157–165.
- [14] Shah, M. M., 1979, "A General Correlation for Heat Transfer During Film Condensation Inside Pipes," *Int. J. Heat Mass Transfer*, **22**, pp. 547–556.
- [15] Hewitt, G. F., Shires, G. L., and Polezhaev, Y. V., Editors, 1997, *International Encyclopedia of Heat and Mass Transfer*, CRC Press, Boca Raton and New York.
- [16] Carey, V. P., 1992, *Liquid-Vapor Phase-Change Phenomena*, Series in Chemical and Mechanical Engineering, Hemisphere Publishing Corporation.
- [17] Palen, J. W., Kistler, R. S., and Frank, Y. Z., 1993, "What We Still Don't Know About Condensation in Tubes," in *Condensation and Condenser Design* J. Taborek, J. Rose, and I. Tanasawa, eds., United Engineering Trustees, Inc. for Engineering Foundation and ASME, New York, pp. 19–53.
- [18] Minkowycz, W. J., and Sparrow, E. M., 1966, "Condensation Heat Transfer in the Presence of Non-Condensibles, Interfacial Resistance, Superheating, Variable Properties, and Diffusion," *Int. J. Heat Mass Transfer*, **9**, pp. 1125–1144.
- [19] *ASHRAE Handbook*, 1985, Fundamentals SI Edition, American Society of Heating, Refrigeration and Air-Conditioning Engineers, Inc., Atlanta, GA.
- [20] Delhaye, J. M., 1974, "Jump Conditions and Entropy Sources in Two-Phase Systems; Local Instant Formulation," *Int. J. Multiphase Flow*, **1**, pp. 395–409.
- [21] Plesset, M. S., and Prosperetti, A., 1976, "Flow of Vapor in a Liquid Enclosure," *J. Fluid Mech.*, **78** (3), pp. 433–444.
- [22] Patankar, S. V., 1980, *Numerical Heat Transfer and Fluid Flow*, Hemisphere, Washington D.C.
- [23] Hirt, C. W., and Nichols, B. D., 1981, "Volume of Fluid (VOF) Method for the Dynamics of Free Boundaries," *J. Comput. Phys.*, **39**, pp. 201–255.
- [24] Sussman, M., Smereka, P., and Osher, S., 1994, "A Level Set Approach for Computing Solutions to Incompressible Two-Phase Flow," *J. Comput. Phys.*, **114**, pp. 146–159.
- [25] Son, G., and Dhir, V. K., 1998, "Numerical Simulation of Film Boiling Near Critical Pressures With a Level Set Method," *ASME J. Heat Transfer*, **120**, pp. 183–192.
- [26] Li, J., and Renardy, Y., 2000, "Numerical Study of Flows of Two Immiscible Liquids at Low Reynolds Number," *SIAM Rev.*, **42**(3), pp. 417–439.
- [27] Yu, G., 1999, "Development of a CFD Code for Computational Simulations and Flow Physics of Annular/Stratified Film Condensation Flows," Ph.D. thesis, ME-EM Department, Michigan Technological University.
- [28] Greenberg, M. D., 1978, *Foundations of Applied Mathematics*, Prentice-Hall, Inc., New Jersey.
- [29] Incropera, F. P., and DeWitt, D. P., 1996, *Fundamentals of Heat and Mass Transfer*, Fourth Edition, Wiley.
- [30] Di Marco, P., Grassi, W., and Trentavizi, F., 2002, "Pool Film Boiling Experiments on a Wire in Low Gravity," in *Microgravity Transport Processes in Fluid, Thermal, Biological, and Material Sciences*, S. S. Sadhal, ed., Annals of the New York Academy of Sciences, **974**, pp. 428–446.